Acta Crystallographica Section A
Foundations of Crystallography
ISSN 0108-7673

Received 31 January 2003
Accepted 20 March 2003

Spectral momentum densities in matter determined by electron scattering[1]

Erich Weigold,* Anatoli S. Kheifets, Vladimir A. Sashin and Maarten Vos

Atomic and Molecular Physics Laboratories, Research School of Physical Sciences and Engineering, Australian National University, Canberra, ACT 0200, Australia. Correspondence e-mail: erich.weigold@anu.edu.au

In electron momentum spectroscopy (EMS), an incoming energetic electron (50 keV in this work) ionizes the target and the scattered and ejected electrons are detected in coincidence (at energies near 25 keV). From the energy and momentum of the detected particles, the energy ω and momentum $\mathbf{q}$ transferred to the target can be inferred. The observed intensity distribution $I(\omega, \mathbf{q})$ is proportional to the spectral momentum density of the target and hence provides a direct challenge to many-body theoretical descriptions of condensed matter. This is illustrated by comparing some many-body calculations with EMS measurements on graphite and polycrystalline aluminium.

1. Introduction

The spectral electron momentum density (SEMD) is an important fundamental property of the electronic structure of a solid. In the independent particle approximation, it gives the probability that an electron in band j has the momentum $\mathbf{q}$ and energy ω (relative to the Fermi energy or vacuum). Electron correlations change this simple picture, introducing a width in the main feature, which varies as a function of $\mathbf{q}$ and ω and is the quasiparticle lifetime. It also introduces density at higher energies, which can be in the form of broad satellite structures (intrinsic plasmons) or broad tails to the main feature (the quasiparticle band) or both.

Although electron momentum spectroscopy (EMS) (Weigold & McCarthy, 1999) gives a direct measurement of SEMD for all materials (from single crystals to amorphous samples), different experimental techniques have been developed to study in detail some aspects of the SEMD. Thus, angle-resolved photoelectron spectroscopy (Hüfner, 1995) provides high-resolution measurements of the energy dependence of occupied states in single crystals. Positron annihilation experiments (West, 1973), which measure the electron–positron pair density, give information on the electron momentum density (EMD) (weighted by the positron wavefunction), but no information on the spectral (energy) dependence. Similarly, Compton scattering, using either photons (Cooper, 1985) or electrons (Williams *et al.*, 1984) as projectiles, gives information on the EMD, although again no information on the energy dependence.

If the ejected recoiling electron is measured in coincidence with the scattered photon or electron and the full collision kinematics is determined, the respective $(\gamma, e\gamma)$ (Bell & Schneider, 2001) or $(e, 2e)$ (McCarthy & Weigold, 1976; Weigold & McCarthy, 1999) measurements allow the reconstruction of the full three-dimensional EMD. Owing to the very much higher cross section for electron–electron scattering than photon–electron scattering, it is possible to resolve energy as well in $(e, 2e)$ measurements and hence the SEMD is fully resolved.

Under EMS conditions, the $(e, 2e)$ collisions involve high-energy incident electrons imparting high momentum transfer to the struck (ejected) electron, so that the incident electron suffers a binary collision with an electron in the target specimen. In the independent particle picture, the binding energy (or separation energy) ω of the target electron is simply the difference in energy between the incoming and two outgoing electrons, and similarly the momentum $\mathbf{q}$ of the target electron *before the collision* is given by the momentum (vector) difference between the sum of the momenta of the two emitted electrons and that of the incident electron. The cross section for seeing such $(e, 2e)$ events is directly proportional to the electron–electron scattering cross section and the probability of an electron having the momentum $\mathbf{q}$ and energy ω. For an interacting many-body system, the latter is given simply by the single-particle spectral function $\rho(\mathbf{q}, \omega)$ (or the spectral momentum density).

$$\sigma(\mathbf{k}_0, \mathbf{k}_1, \mathbf{k}_2; \omega) = (2\pi)^4 \frac{k_1 k_2}{k_0} f_{ee} \rho(\mathbf{q}, \omega), \qquad (1)$$

where $\mathbf{k}_0$, $\mathbf{k}_1$ and $\mathbf{k}_2$ are the momenta of the incident and emitted electrons, and f_{ee} is the electron–electron collision factor, which is essentially constant in the noncoplanar symmetric kinematics employed in our spectrometer (Vos & Weigold, 2000).

The full SEMD is

$$\rho(\mathbf{q}, \omega) = \sum_i |\langle \mathbf{q} | \psi_i \rangle|^2 \pi^{-1} \operatorname{Im} G_i^-(\omega). \qquad (2)$$

[1] Work presented at the Microsymposium on Quantum crystallography, XIX IUCr Congress, Geneva, Switzerland, August 2002.

In writing this expression, we presume that the time-reversed single-particle (or the single-hole) Green function of the many-electron target $G_i^-(\omega)$ can be diagonalized on an appropriate basis of quasiparticle states, and we take the Fourier transform of the one-electron orbital $\psi_i(\mathbf{r})$. In the absence of electron correlations, $\pi^{-1}G_i(\omega) = \delta(\omega - \varepsilon_i)$, where ε_i is the one-electron energy, and the spectrum contains only one δ-function line following the band dispersion.

For a crystal, momentum conservation has also to be satisfied and equation (2) takes the form

$$\rho(\mathbf{q}, \omega) = \sum_{j,\mathbf{k},\mathbf{G}} |\langle \mathbf{q}|\psi_{jk}\rangle|^2 \delta_{\mathbf{q},\mathbf{k}+\mathbf{G}} \pi^{-1} \operatorname{Im} G_j^-(\mathbf{k}, \omega). \qquad (3)$$

Here, j is the band index, $\mathbf{k}$ is the crystal momentum, restricted to the first Brillouin zone, and $\mathbf{G}$ is a reciprocal-lattice vector.

A major problem for EMS applied to condensed matter is the large cross section for incoherent electron scattering in solids. Elastic and inelastic collisions by any of the three continuum electrons can lead to spurious momentum and/or energy changes in the inferred $\mathbf{q}$ and ω, and thus remove events from the true SEMD distribution to other parts of the energy-momentum phase space. Ways of correcting for these multiple scattering effects are discussed by Vos & Bottema (1996) and Weigold & McCarthy (1999). They are minimized by going to high energies and by using very thin (∼100–200 Å) targets. The preparation of ultrathin self-supporting targets is described by Fang *et al.* (1997).

If it is not practicable to make thin targets for transmission experiments, it is possible to use a reflection geometry at low energies on thick targets. Such low-energy $(e, 2e)$ collisions have been used to study the electronic structure of surfaces either with incident electrons normal to the surface (Kirschner *et al.*, 1995; Morozov *et al.*, 2002) or at grazing angles (Rioual *et al.*, 1998; Iacobucci *et al.*, 2000). In these low-energy reflection measurements, multiple scattering effects dominate and the cross sections obtained are no longer directly proportional to the SEMD. Nevertheless, they do yield new insights into the electronic band structures of the samples.

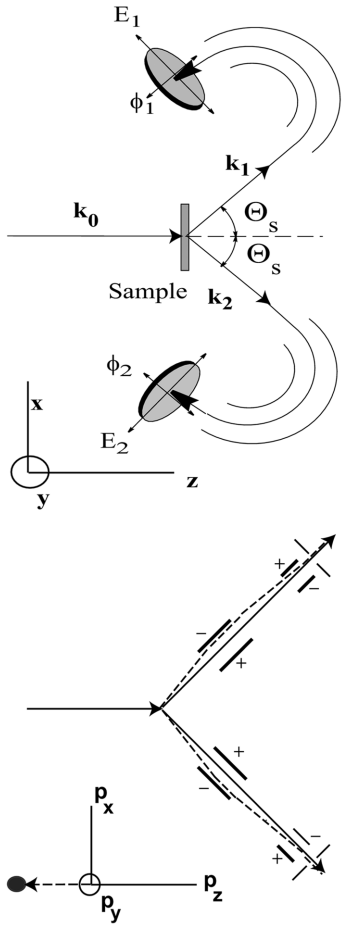

Figure 1
A schematic view of the experiment. Top: a sketch of the incoming and outgoing electrons and the analysers with the two-dimensional detection system. Bottom: the working of the deflectors. The geometry is chosen in such a way that without deflector voltages one measures electrons with $p_x = p_z = 0, p_y \neq 0$. By applying equal voltages, with polarities as indicated we can measure electrons with $p_x = 0, p_z = C, p_y \neq 0$.

2. Experimental technique

The high-energy high-resolution EMS apparatus at the Australian National University has been described in detail by Vos *et al.* (2000) and Vos & Weigold (2000), and so only a brief description will be given here. The incident energy is 50 keV plus an offset to allow for the binding energies. The outgoing electrons pass through two identical hemispherical analysers with equal mean energies ($E_1 = E_2 = 25$ keV) and equal polar angles ($\theta_1 = \theta_2 = 44.3^\circ$). The analysers accept electrons over a range of azimuthal angles, $|\phi_1| \leq 5^\circ$ and $|\phi_2 - \pi| \leq 5^\circ$, where $\phi_1 = 0^\circ = \phi_2 - \pi$ gives the median scattering plane, which is also the horizontal xz plane, where z is along the incident electron direction (see Fig. 1). The electrons transmitted by the analysers are detected with a two-dimensional detector and for each electron the angle and energy are determined. The energy window viewed by each detector is typically 80 eV.

For normal operation with $\theta_1 = \theta_2 = \theta_s = 44.3^\circ$, the momenta $\mathbf{q}$ are measured along the vertical y direction with $q_x = q_z = 0$. By means of sets of double deflector plates placed between the specimen and the acceptance slits to the analysers, it is possible to adjust the operation of the apparatus so that electrons with polar angles $\theta_s \pm \delta\theta_1$ and $\theta_s \pm \delta\theta_2$ are accepted, where $\delta\theta_{1,2}$ are small polar angle variations about 44.3°. This allows one to offset q_x and/or q_z from zero, allowing the SEMD to be measured along a range of q_y values for different fixed q_x and q_z combinations. The observed long-term energy and momentum resolution of this spectrometer is slightly better than 1 eV and 0.1 a.u., respectively. We will in general use atomic units for momenta, where 1 a.u. $\simeq$ 1.89 Å^{-1}.

3. Theoretical calculations

We employ the linear-muffin-tin-orbital (LMTO) method (Skriver, 1986) to write the one-electron wavefunction in a crystal [equation (3)] in the tight-binding representation as the Bloch sum of localized MT orbitals:

$$\psi_{j\mathbf{k}}(\mathbf{r}) = \sum_t \exp(i\mathbf{k}\cdot\mathbf{t}) \sum_\Lambda a_\Lambda^{j\mathbf{k}} \phi_\Lambda(\mathbf{r} - \mathbf{R} - \mathbf{t}). \quad (4)$$

Here **t** is the translation vector and **R** the basis vector. The label Λ defines a MT orbital centred at a given site **R** and it comprises the site index **R** and a set of atomic like quantum numbers. The expansion coefficients $a_\Lambda^{j\mathbf{k}}$ are obtained by solving the eigenvalue problem using the standard variational principle.

The one-hole Green function in equation (3) is calculated by the many-body perturbation theory (MBPT) expansion on the Bloch-wave basis [equation (4)]. Taking the first non-vanishing term leads to the so-called GW approximation (Hedin, 1965; Hedin & Lundqvist, 1969), where G stands for Green's function and W denotes the screened Coulomb interaction. The GW approximation can be improved by introducing vertex corrections in the form of the cumulant expansion to the Green function, which gives calculated plasmon satellite structures in much better agreement with experiment than those predicted by the GW scheme (Aryasetiawan *et al.*, 1996; Vos, Kheifets, Weigold & Aryasetiawan, 2001; Vos, Kheifets, Sashin *et al.*, 2002).

4. Results and discussion

4.1. Graphite

A thin self-supporting single crystal of graphite was prepared by cleaving followed by reactive ion etching in an Ar/O_2 mixture (Fang *et al.*, 1997; Vos *et al.*, 1997). After being transferred under UHV from the preparation chamber to the EMS spectrometer, the sample could be rotated *in situ*. The diffraction pattern of the electron beam transmitted through the graphite sample could be observed on a phosphor screen during the measurements. In this way, we could align the *y* axis of the spectrometer with the $\Gamma - M$ and $\Gamma - K$ direction in the crystal (see Fig. 2). Along the $\Gamma - K$ direction, the maximum (*i.e.* minimal binding energy) in the band is reached at $\simeq 1.3$ a.u., which corresponds to the *M* point in the second Brillouin zone (Fig. 2). Along the $\Gamma - M$ direction, the maximum in the σ band is reached at $q \simeq 1.6$ a.u., which corresponds to the Γ point in the second Brillouin zone. The *xz* plane is a nodal plane of the π band, which therefore has zero density under these conditions ($q_x = q_z = 0$).

In Fig. 3, we show the results of the measurements (Vos, Kheifets, Weigold & Aryasetiawan, 2001; Vos *et al.*, 2003), which are corrected for inelastic multiple scattering as described in Vos, Kheifets & Weigold (2002). The σ band disperses over a larger range in the $\Gamma - M - \Gamma$ direction compared with the $\Gamma - K - M$ direction. At lower binding energies, a hint can be seen of the π band, which is not completely suppressed owing to the finite experimental momentum resolution.

In Fig. 3, we also display the result of our many-body calculation using the cumulant expansion scheme as discussed in the previous section. The calculation is convoluted with a Gaussian of width 1.5 eV, slightly larger than the experimental

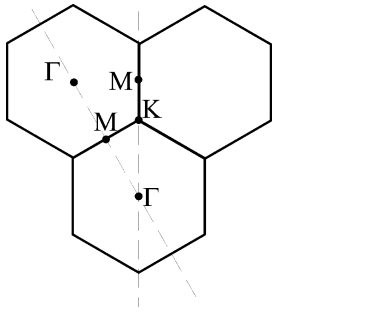

Figure 2
Projection of the Brillouin zones of graphite showing the various symmetry points measured in the experiment. The *y* axis of the spectrometer was aligned with one of the two dashed lines, so that the SEMD could be obtained along these two lines.

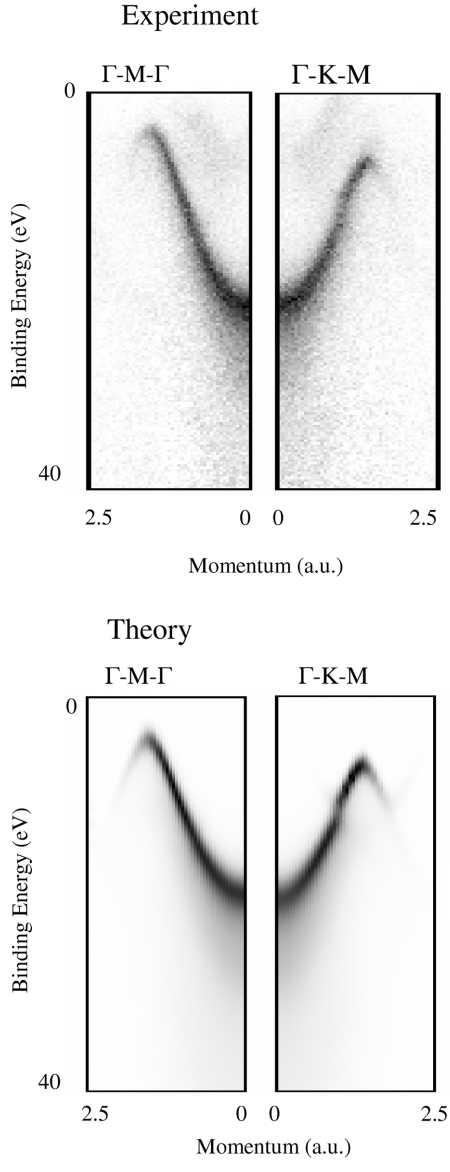

Figure 3
The measured and calculated intensity distributions in two symmetry directions (Fig. 2) in graphite through the Γ point. Darker shades correspond to higher electron densities.

energy resolution of 1.0 eV. This extra energy width gives better agreement with the data. It can perhaps be justified by the fact that we have not included the finite momentum resolution perpendicular to the y axis owing to the time-consuming nature of the calculations.

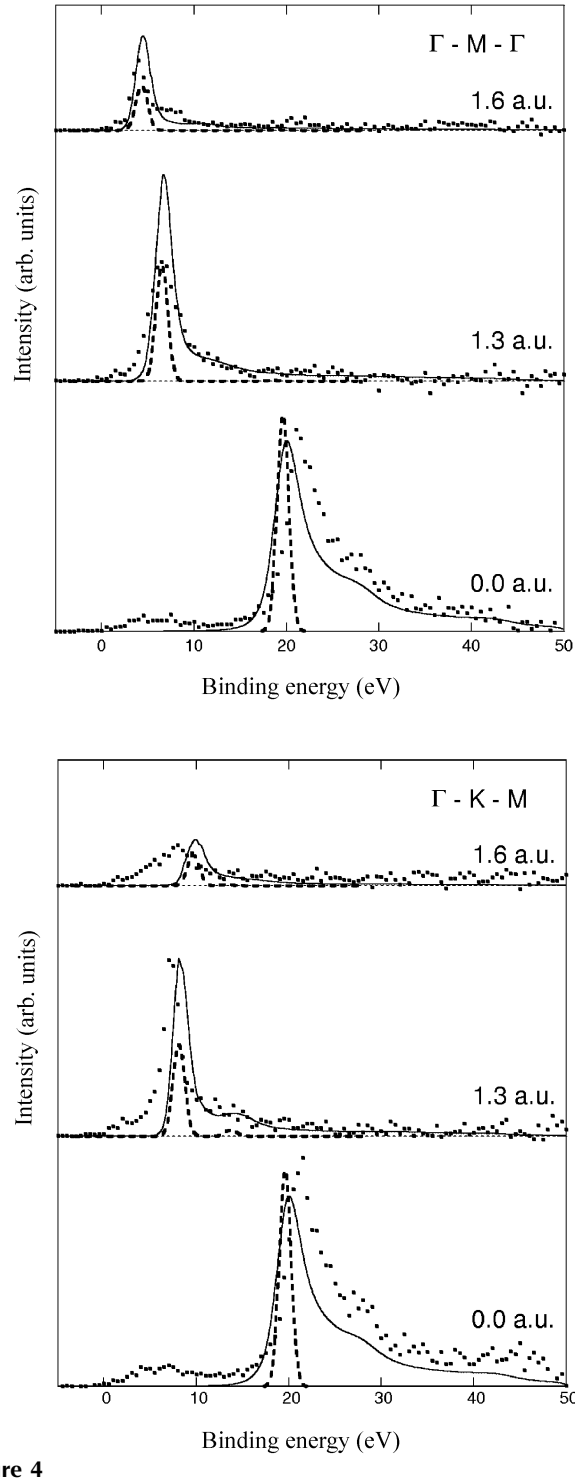

Figure 4
Binding-energy spectra in the two graphite crystal directions at the indicated momenta compared with the LMTO calculations (dashed lines) and the many-body calculation (solid lines). A single normalization factor was used to compare all six measurements with theory.

In the $\Gamma - M - \Gamma$ direction, there is a small band gap in independent-particle (*e.g.* LMTO) band-structure calculations at the Brillouin-zone edge ($\simeq 0.8$ a.u.). This is not resolved, owing to the finite energy resolution and the significant lifetime broadening. However, in the $\Gamma - K - M$ direction, there is a small kink in the dispersion and a notable decrease in intensity at around 0.9 a.u., both in the measurement and in the calculation. This is due to the large (~ 2.5 eV) band gap at the K point (Fig. 2).

Both theory and measurement show significant density below the main dispersing curve, at larger binding energies. This intensity is due to electron–electron correlations as is the width of the dispersing curve at a given momentum (lifetime broadening).

In Fig. 4, we show the binding-energy spectra at momenta of 0, 1.3 and 1.6 a.u. for both orientations of the crystal. Significant asymmetric broadening is seen in the spectrum at zero momentum both in the many-body theory and in experiment. The measurements generally peak at similar (ω, q) values to the calculations. In the measurements and many-body theory, the lifetime broadening decreases with decreasing binding energy. However, as the figure shows, although the theory gives the general features that are observed, the description of the height and width of the structures, *i.e.* the density distribution, is not perfect.

The π band intensity can be observed if we move away from the $q_z = 0$ plane using the deflectors. Fig. 5 shows the spectral density observed along the $\Gamma - M$ direction (as in Fig. 3) in the left panel and in the right panel the spectral density observed along the same line but shifted along the $\Gamma - A$ direction by 0.5 a.u. The dispersive intensity distribution owing to the π band is clearly visible at small binding energy in the right panel. Again, this band shows significant lifetime broadening. Also clearly visible in Fig. 5 is that the σ band shows very little dispersion in the $\Gamma - A$ direction, the bottom of the band moving to smaller binding energy by only about 1.5 eV.

4.2. Aluminium

The measured SEMD of occupied states in the conduction band and the 2p core level of polycrystalline aluminium is shown in Fig. 6 as a grey-scale intensity plot (Kheifets *et al.*, 2001). The top panel shows the raw data and the bottom panel shows the same data after deconvolution of inelastic events using the measured energy-loss spectra obtained for the same sample as discussed by Vos, Kheifets, & Weigold (2001). The 'free-electron' dispersion in the valence band and the associated broad high-energy (satellite) contribution is clearly visible. The 2p core level, on the other hand, shows no dispersion and is far more extended in momentum space. Its momentum distribution can be accurately fitted by a Hartree–Fock atomic Al 2p wavefunction (Kheifets *et al.*, 2001, 2004; Vos, Kheifets, & Weigold, 2001), which has a node (zero intensity) at $q = 0$. Besides the broad tail and satellite structure in the valence region owing to electron correlations, the other noticeable feature of the measured SEMD is that the peak density is not uniform along the band. At zero

momentum (a Γ point), the peak density is significantly lower than in the arms of the band. This is a result of the quasiparticle lifetime being much shorter around the Γ point than nearer to the Fermi level.

A detailed comparison of cumulant expansion calculation for Al and the measurements is shown in Figs. 7 and 8. In Fig. 7, the calculation has been convoluted with calculated multiple scattering effects due to both elastic and inelastic scattering using the Monte Carlo simulation technique of Vos & Bottema (1996). Fig. 7 shows slices through the SEMD at the selected energies. The momentum profiles at given energies (relative to the Fermi energy) are well described by the many-body calculations, in terms of both the shapes of the profiles and the peak heights. The small amount of density above the Fermi energy is due to the finite energy resolution.

Fig. 8 shows binding-energy spectra at selected momenta. Here we used a slightly different approach for comparing the data with theory. The experimental data were deconvoluted for inelastic energy-loss events, using the measured energy-loss distribution. In this way, one can correct for inelastic energy-loss processes, without any free parameters, as explained in Vos, Kheifets & Weigold (2002). The structures in the binding-energy spectra (Fig. 8) are much broader than the energy resolution of 1 eV. The main feature is a broad peak dispersing as a free electron from $\omega \sim 11$ eV at $q = 0$ to $\omega = 0$ at the Fermi edge ($q \sim 0.9$ a.u.). The broadening of this main quasiparticle peak owing to its short lifetime is well reproduced by the many-body calculation. The peak density has a minimum at $q = 0$, where the width is the greatest, and a maximum at $q \sim 0.65$ a.u.

The calculation is directly compared with the deconvoluted measurement and it reproduces quite well the widths, peak positions and heights of the main quasiparticle contribution at the different momenta. Thus, elastic multiple-scattering effects, not corrected for in the latter approach, are quite minor.

The intensity above the quasiparticle peak, after deconvolution for inelastic energy loss, is thus also due to many-body effects, as it is visible in both theory and experiment. It has a broad maximum that is separated from the quasiparticle peak by the well defined plasmon energy ($\simeq 15$ eV) and hence the simple picture that this intensity is due to creation of intrinsic plasmons explains its position but not its excess width.

The momentum dependency of this satellite structure is, however, quite different to that of the main quasiparticle peak. Relative to a quasiparticle intensity of 1, the measured

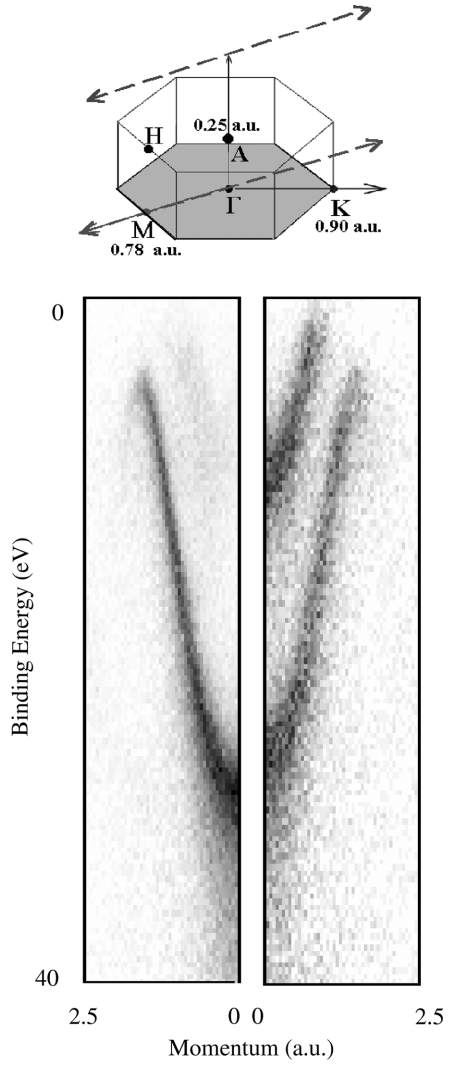

Figure 5
The measured spectral momentum density in graphite along the $\Gamma - M$ direction (left panel) and the same direction but offset by 0.5 a.u. along the $\Gamma - A$ axis (right panel).

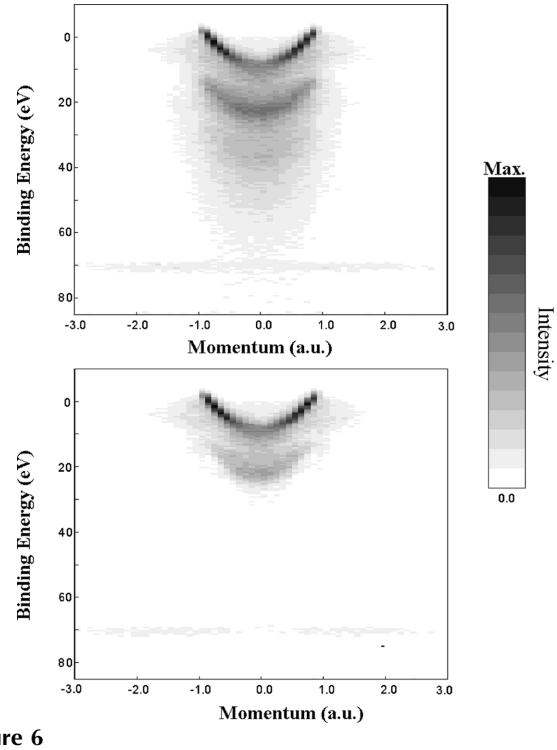

Figure 6
The measured SEMD for polycrystalline aluminium (Kheifets *et al.*, 2001) before (top) and after (bottom) deconvolution of inelastic multiple scattering. The 2*p* core band is at around 70 eV. The density is shown on a linear grey scale.

(calculated) satellite intensity decreases from ~ 0.73 (0.63) at $q \sim 0$ to 0.43 (0.46) at $q \sim 0.65$ a.u. and 0.27 (0.32) near the Fermi edge ($q \sim 0.85$ a.u.). The calculated 'satellite' intensity varies with momentum in approximate agreement with the measurements. However, it gives a somewhat broader structure, peaking at slightly higher binding energies compared with experiment.

5. Summary

Measurements of the SEMD of graphite with $q_{\Gamma-A} = 0$, *i.e.* with zero momentum perpendicular to the graphite plane, show that the π electrons have zero density in this plane and also quite clearly resolve the anisotropy between the $\Gamma - M - \Gamma$ and $\Gamma - K - M$ directions for σ electrons. At any given momentum, substantial lifetime broadening is seen for the σ band, with maximum broadening at the bottom of the band at $q = 0$ (Γ point). This broadening is asymmetric with a high energy tail in the binding-energy spectrum.

The shape of the SEMD, both lifetime broadening and dispersion, is quite well reproduced by our many-body cumulant expansion calculation. When a slice is taken through the SEMD with a $q_{\Gamma-A} = 0.5$ a.u. offset, the π band becomes very prominent and the σ band is seen to show little dispersion in the $\Gamma - A$ direction.

In the case of aluminium, the SEMD shows that its electronic structure is much more complicated than implied by its description as a 'free-electron' metal. Correlation effects are seen to be dominant, giving rise to very significant lifetime broadening in the main quasiparticle dispersive structure and to intense broad satellite structure which peaks at around 15 eV above the quasiparticle peak. The intensity of this 'satellite' structure has a different momentum dependence compared with that for the main quasiparticle peak. All these features are again quite well described by our cumulant expansion many-body theoretical calculations, although it does give the satellite peak at an energy that is a little too high. In general, the main features of the SEMD of both graphite and aluminium can be quite well understood through the

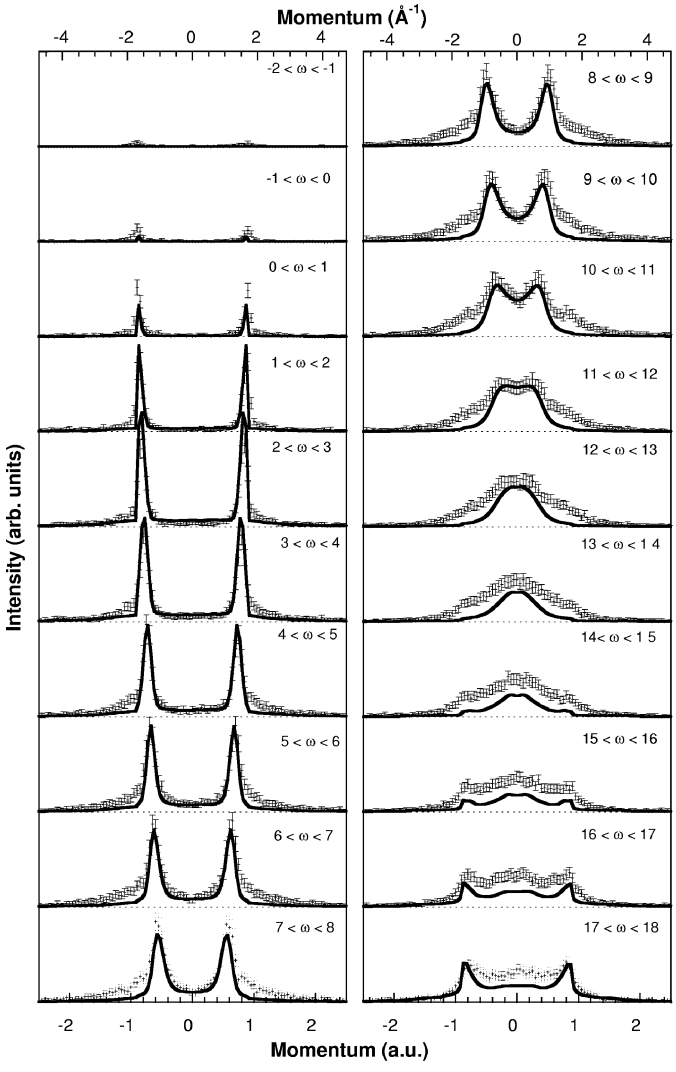

Figure 7
Momentum profiles at different binding energies relative to the Fermi level for aluminium. The solid line is the cumulant expansion many-body calculation corrected for elastic multiple scattering.

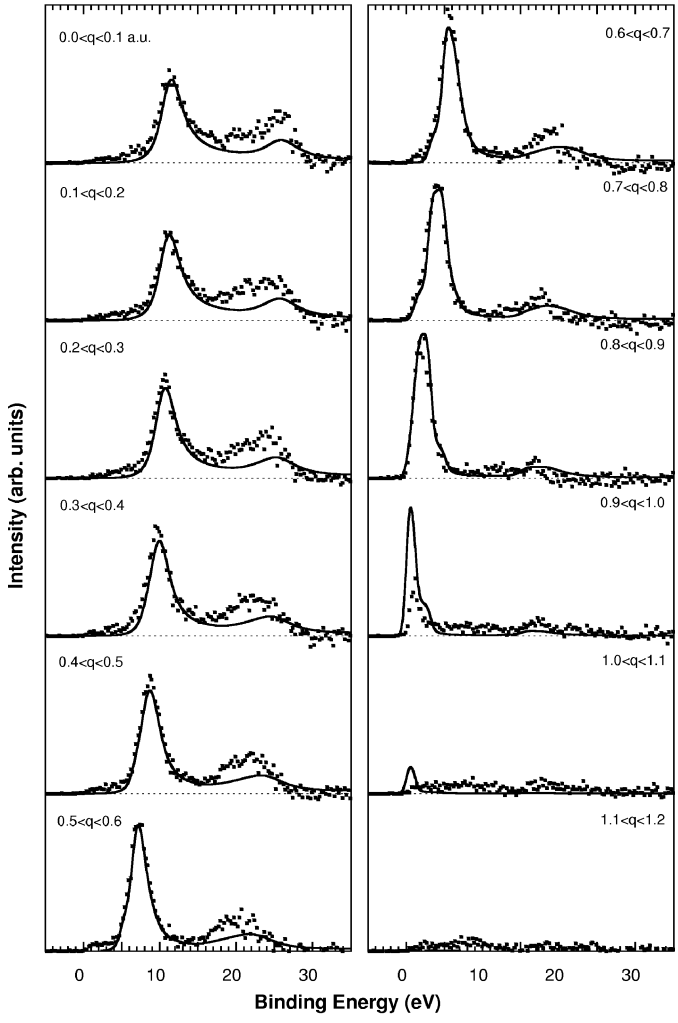

Figure 8
The measured SEMD for aluminium, deconvoluted for inelastic energy loss, compared with the many-body cumulant expansion theory (solid line) for the momentum values as indicated.

cumulant expansion approximation to the many-body interaction problem.

References

Aryasetiawan, F., Hedin, L. & Karlsson, K. (1996). *Phys. Rev. Lett.* **77**, 2268–2271.

Bell, F. & Schneider, J. R. (2001). *J. Phys. Condens. Matter*, **13**, 7905–7922.

Cooper, M. (1985). *Rep. Prog. Phys.* **48**, 415–481.

Fang, Z., Guo, X., Utteridge, S., Canney, S. A., McCarthy, I. E. & Weigold, E. (1997). *Rev. Sci. Instrum.* **68**, 4396–4403.

Hedin, L. (1965). *Phys. Rev.* **139**, A796–A823.

Hedin, L. & Lundqvist, S. (1969). *Solid State Phys.* **23**, 1–181.

Hüfner, S. (1995). *Photoelectron Spectroscopy*. Berlin: Springer.

Iacobucci, S., Ruocco, A., Rioual, S., Mastropietro, A. & Stefani, G. (2000). *Surf. Sci.* **454–456**, 1026–1030.

Kheifets, A. S., Vos, M. & Weigold, E. (2001). *Z. Phys. Chem.* **215**, 1323–1339.

Kheifets, A. S., Vos, M. & Weigold, E. (2004). In *Handbook of Aluminium*, edited by D. MacKenzie & G. Totten. New York: Marcel Dekker.

Kirschner, J., Artamonov, O. M. & Samarin, S. N. (1995). *Phys. Rev. Lett.* **75**, 2424–2427.

McCarthy, I. E. & Weigold, E. (1976). *Phys. Rep.* **27C**, 275–371.

Morozov, A., Berakdar, S., Samarin, S. N., Hillebrecht, F. U. & Kirschner, J. (2002). *Phys. Rev. B*, **65**, 104425-1–104425-10.

Rioual, S., Iacobucci, S., Neri, D., Kheifets, A. S. & Stefani, G. (1998). *Phys. Rev. B*, **57**, 2545–2549.

Skriver, H. (1986). *The LMTO Method*. Berlin: Springer Verlag.

Vos, M. & Bottema, M. (1996). *Phys. Rev. B*, **54**, 5946–5954.

Vos, M., Cornish, G. P. & Weigold, E. (2000). *Rev. Sci. Instrum.* **71**, 3831–3840.

Vos, M., Fang, Z., Canney, S., Kheifets, A. S., McCarthy, I. E. & Weigold, E. (1997). *Phys. Rev. B*, **56**, 963–966.

Vos, M., Kheifets, A. S., Sashin, V. A. & Weigold, E. (2003). *X-ray and Inner-Shell Processes*, *AIP Conference Proceedings*, No. 652, edited by A. Biancini, A. Marcelli & N. L. Saini, pp. 491–496. New York: American Institute of Physics.

Vos, M., Kheifets, A. S., Sashin, V. A., Weigold, E., Usuda, M. & Aryasetiawan, F. (2002). *Phys. Rev. B*, **66**, 155414.

Vos, M., Kheifets, A. S. & Weigold, E. (2001). *J. Phys. Chem. Solids*, **62**, 2215–2221.

Vos, M., Kheifets, A. S. & Weigold, E. (2002). In *Correlations, Polarization and Ionization in Atomic Systems*, *AIP Conference Proceedings*, No. 604, edited by D. H. Madison & M. Schulz, pp. 70–75. New York: American Institute of Physics.

Vos, M., Kheifets, A. S., Weigold, E. & Aryasetiawan, F. (2001). *Phys. Rev. B*, **63**, 033108-1–033108-4.

Vos, M. & Weigold, E. (2000). *J. Electron Spectrosc. Relat. Phenom.* **112**, 93–106.

Weigold, E. & McCarthy, I. E. (1999). *Electron Momentum Spectroscopy*. New York: Kluwer Academic/Plenum.

West, R. N. (1973). *Adv. Phys.* **22**, 263–283.

Williams, B. G., Sparrow, T. G. & Egerton, R. F. (1984). *Proc. R. Soc. London Ser. A*, **393**, 409–422.